RESEARCH ARTICLE

In vitro post-stenotic flow quantification and validation using echo particle image velocimetry (Echo PIV)

Andrew M. Walker · Joel Scott · David E. Rival ·
Clifton R. Johnston

Abstract Echo particle image velocimetry (Echo PIV) presents itself as an attractive in vivo flow quantification technique to traditional approaches. Promising results have been acquired; however, limited quantification and validation is available for post-stenotic flows. We focus here on the comprehensive evaluation of in vitro downstream stenotic flow quantified by Echo PIV and validated in relation to digital particle image velocimetry (DPIV). A Newtonian blood analog was circulated through a closed flow loop and quantified immediately downstream of a 50 % axisymmetric blockage at two Reynolds numbers (Re) using time-averaged Echo PIV and DPIV. Centerline velocities were in good agreement at all Re; however, Echo PIV measurements presented with elevated standard deviation (SD) at all measurements points. SD was improved using increased line density (LD); however, frame rate or field of view (FOV) is compromised. Radial velocity profiles showed close agreement with DPIV with the largest disparity in the shear layer and near-wall recirculation. Downstream recirculation zones were resolved by Echo PIV at both Re; however, magnitude and spatial coverage was reduced compared to DPIV that coincided with reduced contrast agent penetration beyond the shear layer. Our findings support the use of increased LD at a cost to FOV and highlight reduced microbubble penetration beyond the shear layer. High local SD at near-wall measurements suggests that further refinement is required before proceeding to in vivo quantification studies of wall shear stress in complex flow environments.

1 Introduction

Accurate quantification of arterial near-wall flow patterns and wall shear stress (WSS) is critical if we are to predict sites susceptible to intimal thickening and atherosclerotic development. Once thought to be associated with high WSS, sites prone to hyperplasia have been linked to low and oscillating WSS corresponding with complex flow patterns at vessel bifurcations and downstream of stenotic vessels (Malek et al. 1999; Wootton and Ku 1999; Stroud et al. 2002). Although several diagnostic approaches are available for the quantification of in vivo flows, precise evaluation of near-wall flow and WSS remains a challenging endeavor (Zhang et al. 2011).

Pulse wave Doppler (PWD) allows for quantification of flow within a measured sample volume. However, this is limited to centerline velocity acquisition that necessitates extrapolation of a parabolic velocity profile to the wall for WSS calculation. Along with an oversimplification of the velocity profile, PWD is restricted by one dimension velocity extraction, high angle dependence and spectral broadening. Phase-contrast magnetic resonance imaging (PC-MRI) provides high spatial resolution imagery; however, in vivo application is restricted by poor temporal resolution, long scan times, high costs and breath holds. Ultrasound-based approaches have also been developed including plane wave excitation (PWE) (Udesen et al. 2008), ultrasound speckle velocimetry (USV) (Bohs et al. 1995, 2000) and ultrasonic perpendicular velocimetry (UPV) (Beulen et al. 2010a, b). USV tracks speckle

A. M. Walker (✉) · D. E. Rival
Department of Mechanical and Manufacturing Engineering,
University of Calgary, 2500 University Dr. NW, Calgary,
AB T2N 1N4, Canada
e-mail: walkeram@ucalgary.ca

J. Scott · C. R. Johnston
Department of Mechanical Engineering, Dalhousie University,
PO Box 15000, Halifax, NS B3H 4R2, Canada

patterns within the interrogated flow field. Although removing the constraint of angle dependence, this approach does require the use of high seeding density to induce strong scattering that restricts in vivo application (Bohs et al. 1995, 2000; Kim et al. 2004a; Beulen et al. 2010a). UPV cross-correlates speckles from ultrasound radio frequency (RF) data to quantify velocity perpendicular to the beam (Beulen et al. 2010a). Although yet to be applied to in vivo flows, UPV is a potential attractive approach that does not necessitate contrast agent infusion and provides for excellent radial resolution (Beulen et al. 2010a). However, interrogation window size is large in the axial direction reducing axial resolution while the low echogenicity of red blood cells may degrade the signal to noise ratio (Zhang et al. 2011).

Echo particle image velocimetry (Echo PIV) has presented itself as an attractive diagnostic alternative for in vivo flow quantification. Echo PIV strives to take two unconnected flow investigatory approaches (PIV and ultrasound) to improve upon the above-mentioned deficiencies using relatively low cost equipment in a high spatial and temporal resolution imaging environment. This approach pairs PIV with the use of contrast agents and ultrasound imaging to allow for the investigation of opaque flows. To date, promising in vitro results have been acquired by Kim et al. (2004a, b), Zheng et al. (2006), Liu et al. (2008) and Zhang et al. (2008) in comparison to optical PIV, PWD and CFD models. Furthermore, this approach has been applied in vivo to the investigation of rotational flow in a stented thoracic aorta (Dobson et al. 2007, 2009), left ventricular flow (Sengupta et al. 2007; Hong et al. 2008; Kheradvar et al. 2010) and a validation of carotid artery flow both in rats and humans with PWD (Niu et al. 2010) and PC-MRI (Zhang et al. 2011), respectively. However, application to complex flow environments, specifically, stenotic induced flow has been minimal. Qian et al. (2011) and Zhu et al. (2011) quantified flow downstream of an axisymmetric blockage to PWD and computational fluid dynamic modeling (CFD), respectively. Close agreement was found between Echo PIV and the validation approaches; however, quantification was limited strictly to maximum centerline comparison and velocity vector and contour maps. Qian et al. (2010) also measured flow downstream of a 25 % by diameter stenosis fabricated in a 0.6 mm diameter tube, here termed micro-EPIV. Micro-EPIV measured centerline values displayed a good fit to PWD; however, downstream recirculation was not resolved and near-wall velocities were overestimated in relation to CFD predictions (Qian et al. 2010). Liu et al. (2008) commented on good agreement between Echo PIV and PWD measured centerline velocities; however, no quantitative comparison was presented. Although PWD is appropriate for centerline validation, reliance on a parabolic velocity profile

extrapolation renders this approach unsuitable as a gold standard for near-wall flow and WSS quantification. Additionally, the use of CFD is challenging in transitional/turbulent environments that can be associated with separated flows (Young et al. 2007). Although the qualitative merits of Echo PIV can be well appreciated, a comprehensive analysis of its capabilities and limitations in complex flow is required before endorsing its use as an effective quantitative tool in these environments (Poelma et al. 2012).

We present an experimental comparison of downstream stenotic induced flow through a 50 % by area axisymmetric blockage at two Reynolds numbers (Re) using Echo PIV and digital PIV (DPIV). Our aim was to comprehensively quantify downstream flow through comparison of axial velocity and negative axial velocity profiles, centerline velocities and radial velocity profiles that are important predictors in resulting WSS patterns. The measurable dynamic range of Echo PIV is inherently linked to frame rate (FR), field of view (FOV) and beam line density (LD) (Liu et al. 2008). Acquiring high velocities requires a high FR that comes at a cost of reduced FOV or LD that represent the number of vertical scan lines that comprise the FOV (Curry et al. 1990). We sought to determine whether increased LD while maintaining FR at a cost to FOV resulted in improved agreement with DPIV measurements. Given the small diameter and favorable density of the contrast agent in relation to the circulating fluid, it was expected that added microbubbles would faithfully follow the flow allowing complex patterns induced by the blockage to be resolved by Echo PIV.

2 Methods

2.1 Flow conditions

A closed flow loop permitting ultrasound interrogation and optical access was constructed to mimic the arterial circulation (Figs. 1a, b, 2). The test section consisted of a 0.635 cm radius (R) (0.158 cm wall thickness) extruded acrylic tube (Laird Plastics, Calgary, AB, Canada) housed in an acrylic flow chamber filled with deionized water. A Newtonian blood analog of 40 % by volume glycerol and deionized water (viscosity (μ) = 3.8 cP, density (ρ) = 1,070 kg/m^3) was driven through the loop in steady state conditions by a ISMATEC Reglo-Z digital gear pump (Cole Parmer, Montreal, QC, Canada) using a GJN-25 Micropump pump head (Cole Parmer). Although arterial flow is distinctly pulsatile, the use of steady state conditions reduces the added parameter space that accompanies the use of a complex flow wave allowing for a better understanding of the capabilities and limitations of Echo PIV in a already complex flow environment.
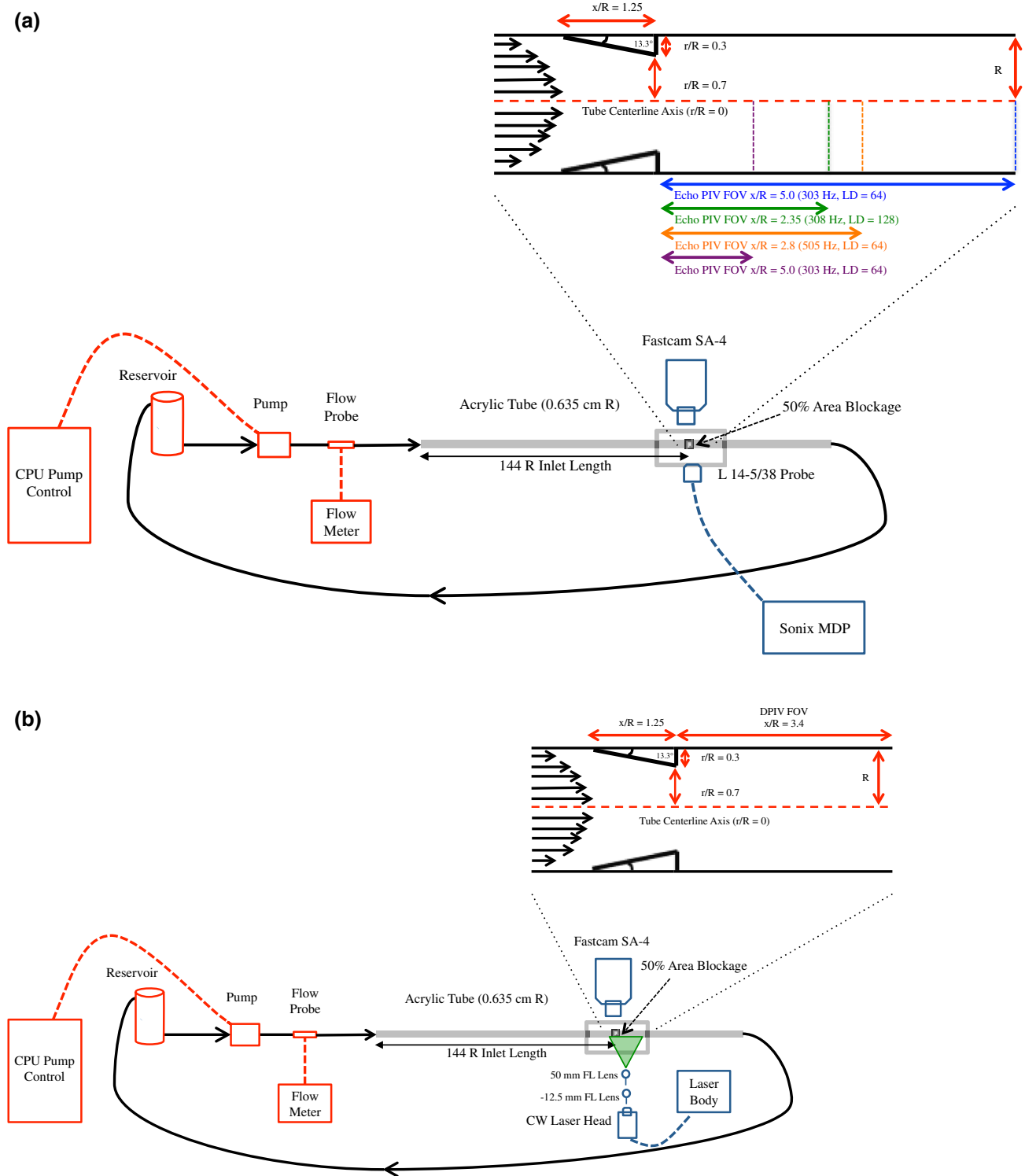
(a)

x/R = 1.25
13.3°
r/R = 0.3
r/R = 0.7
Tube Centerline Axis (r/R = 0)
R

Echo PIV FOV x/R = 5.0 (303 Hz, LD = 64)
Echo PIV FOV x/R = 2.35 (308 Hz, LD = 128)
Echo PIV FOV x/R = 2.8 (505 Hz, LD = 64)
Echo PIV FOV x/R = 5.0 (303 Hz, LD = 64)

Fastcam SA-4

Reservoir
Pump
Flow Probe
Acrylic Tube (0.635 cm R)
50% Area Blockage

CPU Pump Control

Flow Meter

144 R Inlet Length
L 14-5/38 Probe

Sonix MDP

(b)

DPIV FOV
x/R = 3.4
x/R = 1.25
13.3°
r/R = 0.3
r/R = 0.7
Tube Centerline Axis (r/R = 0)
R

Fastcam SA-4
50% Area Blockage

Reservoir
Pump
Flow Probe
Acrylic Tube (0.635 cm R)

CPU Pump Control

Flow Meter

144 R Inlet Length

50 mm FL Lens
-12.5 mm FL Lens
CW Laser Head

Laser Body

Fig. 1 Schematic representation of echo particle image velocimetry (Echo PIV) (**a**) and digital particle image velocimetry (DPIV) (**b**) experimental closed flow loop setups with corresponding stenotic geometry and downstream extent of field of view (FOV)

Reynolds numbers of 320 and 520 representative of mean values associated with the carotid artery and abdominal aorta were investigated that corresponded to flow rates of 10.6 and 17.8 mL/s, respectively (Walburn et al. 1981; Moore et al. 1992, Ku 1997). An entrance length of 144 R from the proximal end of the acrylic tube
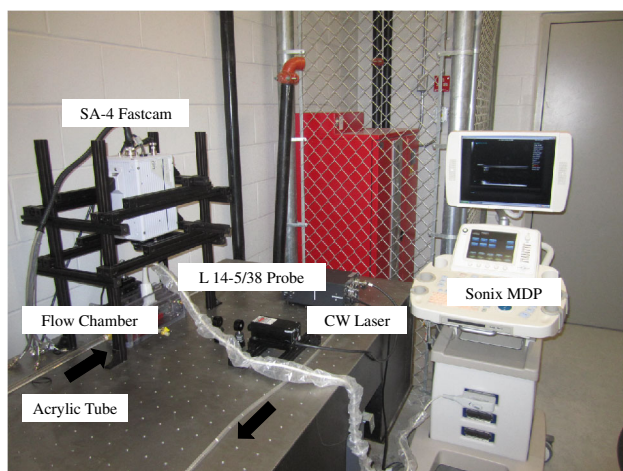
Fig. 2 Experimental closed flow loop setup demonstrating ultrasound and digital particle image velocimetry (DPIV) interrogation (*arrows* indicate flow direction)

to our area of flow interrogation ensured fully developed flow at all *Re* (Eq. 1):

$$\frac{L}{D} = \left(0.619^{1.6} + 0.0567 Re^{1.6}\right)^{\frac{1}{1.6}} \tag{1}$$

where $\frac{L}{D}$ is the required entrance length in pipe diameters (see Durst et al. 2005). Upon acquisition of initial measurements, the acrylic tube was cut whereupon an axisymmetric stainless steel blockage was introduced into the tube at a distance of 144 *R* from the proximal inlet. The inserted blockage was cut to a length of $x/R = 1.25$ from a larger rod of stainless steel with a prefabricated inner area reduction of ~ 50 % (radial reduction of $r/R = 0.3$). The two pieces of cut acrylic were subsequently appended, enveloping the blockage housed within the core of the tube. The inlet of the blockage was beveled in order to reduce upstream flow effects and delay flow separation until the expansion region at the blockage outlet. Downstream Echo PIV and DPIV measurements were acquired at inlet *Re* of 320 and 520.

2.2 Echo PIV measurements

Initial Echo PIV measurements were acquired prior to blockage insertion for comparison to known analytical theory and DPIV acquired measurements. The experimental setup necessitated Echo PIV and DPIV measurement acquisition on sagittal and coronal planes, respectively (see limitation). B-mode time-averaged images at FR = 203 and 340 Hz corresponding to measurements at $Re = 320$ and $Re = 520$ were acquired using Sonix MDP hardware with an L 14-5/38 linear probe (Ultrasonix, Richmond, BC, Canada) at 10 MHz (Table 1). The acquisition of one hundred images was found to be

Table 1 Echo particle image velocimetry (Echo PIV) imaging parameters

Parameter	Description
Ultrasound Hardware	Ultrasonix Sonix MDP
Transducer	L 5-14/38
	Frequency: 10 MHz
Tracer particles	Definity® echo contrast
	Perflutren lipid microspheres
	(1.1–3.3 μm, Perflutren, liquid (20 °C) = 1,350 kg/m³)
Axial resolution	0.23 mm
Lateral resolution	0.5 mm
Slice thickness	~ 1.61 mm
Depth	3.1 mm
Beam line density (LD)	0.5 (64 LD), 1.0 (128 LD)
Stokes number (St_{EchoPIV})*	$Re \sim 320 \cong 6.5 \times 10^{-5}$, $Re \sim 520 \cong 1.1 \times 10^{-4}$
Image separation time	$\sim 3{,}280$ μs at $Re \sim 320$, $\sim 1{,}960$ μs at $Re \sim 520$
Correlation algorithm	Adaptive multipass, final interrogation window size 32 × 32 with 75 % window overlap

* $St_{\text{EchoPIV}} = \frac{\tau_s}{\tau_{\text{EchoPIV}}}$ where τ_s is the particle relaxation time equal to $\tau_s = dp^2 \frac{\rho p^2}{18\mu}$ where ρp^2 is the density of the particles, dp^2 is the diameter of the particles and μ is the viscosity of the circulating Newtonian fluid. τ_{EchoPIV} is the finite time separation between two observations (separation time between ultrasound image snapshots)

sufficient for the convergence of velocity data. A single focus was placed approximately equidistant between the centerline and the far wall of the acrylic tube at a distance of 3.1 cm from the transducer. Definity® ultrasound contrast agent (Lantheus Medical Imaging, N. Billerica, MA, USA) with a density approximate to that of blood (Becher and Burns 2000) was diluted in normal saline and injected into the reservoir upstream of our arterial model. Micro-bubble seeding concentrations followed that described previously with a final bubble concentration of $\sim 2 \times 10^3$ mL^{-1} (Liu et al. 2008; Niu et al. 2011). Upon blockage insertion, B-mode time-averaged images were subsequently acquired immediately downstream of the outlet at two LD (Fig. 3a). Similar to pre-blockage flow, satisfactory convergence of the velocity field was achieved upon acquisition of 100 images. Frame rates of 303 and 308 Hz at LD 64 and LD 128 were used to acquire images at $Re = 320$. The inherent link between FR, FOV and LD necessitated a reduction in sector size resulting in downstream FOVs of $x/R = 5.0$ for LD 64 and $x/R = 2.35$ for LD 128 (Fig. 1a). Frame rates were increased to 505 and 520 Hz for LD 64 and LD 128 at $Re = 520$. Subsequent sector sizes were reduced to $x/R = 2.8$ and $x/R = 1.3$, respectively (Fig. 1b).
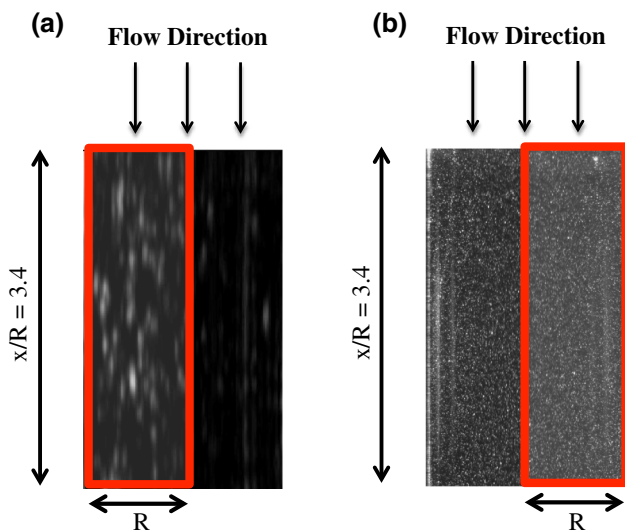
Fig. 3 Representative echo particle image velocimetry (Echo PIV) (**a**) and digital particle image velocimetry (DPIV) (**b**) acquired images at $Re = 320$ downstream of a 50 % reduction by area axisymmetric blockage. Definity® echo contrast and silver coated hollow glass spheres were added to Echo PIV and DPIV interrogated flows, respectively. Shaded red boxes represent study FOVs. For the purposes of display, the Echo PIV image has been rotated 90° to match the orientation of the DPIV image

Sets of B-mode files at each LD and Re were transferred to MATLAB R2011a software (MathWorks, Natick, MA, USA) for image generation. Generated images were imported to DaVis 8.1.3 software (LaVision GmbH, Goettingen, Germany) for PIV quantification using a multi-pass, iterative FFT-based cross-correlation algorithm. Initial interrogation window size was 128×128 pixels whereupon subsequent refinements generated a final window size of 32×32 pixels with 75 % overlap. The selected cross-correlation algorithm calculates a complex 2D-FFT from the interrogation window. Inherently, the FFT-based cross-correlation introduces a weighting function that accentuates pixel displacements of (0,0) with decreased weighting applied to larger displacements. The use of multi-pass iterative cross-correlation as was used here, opposed to a single-pass approach, serves to eliminate this bias as subsequent grid refinements from the initial pass limit displacement to ±1 pixel. Additionally, correlation errors are heightened within interrogation windows that envelope high velocity gradient flow that is to be expected downstream of a stenotic constriction. PIV algorithms assume uniform particle displacement within interrogation areas, which becomes problematic in the shear layer. This translates into correlation peak broadening that increases the likelihood of spurious vectors and measurement bias (Meunier and Leweke 2003; Raffel et al. 2007). However, this can be remedied to a degree through the use of a multi-grid-iterative correlation algorithm as

was used here (Theunissen et al. 2007; Xiong and Chong 2007; Raffel et al. 2007).

Near-field reverberations necessitated image pre-processing using average background intensity subtraction. An average intensity image was generated that was subsequently subtracted from each individual B-mode image. Despite pre-processing, the residual presence of near-field noise restricted PIV quantification from the tube centerline to the far wall. The resulting individual and vector averaged velocity fields presented with 19 radially spaced vectors at all LD and Re equating to a final Echo PIV spatial vector grid of $\sim 0.33 \times 0.33$ mm² and where axial vector extent was dependent on sector size. Smoothing was not applied to the Echo PIV vector fields. Echo PIV individual vector fields and the final time-averaged vector field were exported for post-processing in MATLAB R2011a.

The temporal separation of successive B-mode images is a function of both FR and horizontal displacement as scan lines encompassing the FOV are not acquired simultaneously (Poelma et al. 2011). As such, all acquired Echo PIV axial velocities were subjected to a sweep correction (Eq. 2) as detailed by Poelma et al. (2011):

$$U_x = \frac{M\Delta x}{\frac{1}{FR} + \frac{\Delta x}{\gamma}} \tag{2}$$

where U_x is the corrected axial velocity, M is a scaling factor converting pixels to distance, Δx is axial pixel displacement, FR is frame rate and γ is sweep speed. As noted by Poelma et al. (2011), ultrasound sweep correction becomes increasingly noteworthy upon acquisition at slower sweep speeds or for larger images. Wall noise and light reverberations necessitated the removal of the first axial measurement radially from the wall where relative errors become large (Hochareon et al. 2004; Kähler et al. 2006; Peterson and Plesniak 2008). Furthermore, Echo PIV measurements from the blockage outlet to $x/R = 0.2$ were omitted on the account of correlation degradation due to air bubble deposition immediately downstream of the blockage.

2.3 DPIV measurements

DPIV time-averaged images were acquired using a Fastcam SA-4 camera (Photron, San Diego, CA, USA, $1,024 \times 1,024$ pixel full resolution) of the circulating fluid seeded with 15 µm silver coated hollow glass sphere tracer particles (Potters Industries Inc., Carlstadt, NJ, USA) and illuminated using a continuous wave 532 nm 1 W green laser (Dragon Lasers, Changchun, Jilin, China) (Table 2). Cylindrical optics generated a laser sheet with a thickness of approximately 1.5 mm. Images were acquired in single frame mode at FR of 1,500 and 2,500 Hz for $Re = 320$ and

Table 2 Digital particle image velocimetry (DPIV) imaging parameters

Parameter	Description
Laser	Dragon lasers solid state 1-W CW Laser, 532 nm
	Output Power: >1,000 mW
	Sheet thickness at FOV: 1.5 mm
Laser sheet optics	−12.5 mm FL cylindrical lens
	50 mm FL cylindrical lens
Camera	Photron SA-4
	Single frames per second: 3,600 Hz full resolution
	Pixel ($h_x v$): 1,024 × 1,024
	Pixel size ($h_x v$): 20 µm × 20 µm
	Active area ($h_x v$): 20.48 mm × 20.48 mm
Camera lens	Nikon AF Micro Nikkor 60 mm f/2.8D
Tracer particles	Silver coated hollow glass spheres (15 µm, 1,600 kg/m^3)
Stokes number (St_{PIV})*	$Re \sim 320 = 0.012$, $Re \sim 520 = 0.019$
FOV ($h_x v$)	Prior to masking: 26 mm × 26 mm
F#	32
Diffraction limited diameter	69.0 µm
Minimum possible image size	71.9 µm
Image size in pixels	3.6
Image separation time	500 µs at $Re \sim 320$, 277 µs at $Re \sim 520$
Correlation algorithm	Adaptive multipass, final interrogation window size 32 × 32 with 75 % window overlap

* $St_{PIV} = \frac{\tau_s}{\tau_{PIV}}$ where τ_s is the particle relaxation time equal to $\tau_s = dp^2 \frac{\rho p^2}{18\mu}$ where ρp^2 is the density of the particles, dp^2 is the diameter of the particles and μ is the viscosity of the circulating Newtonian fluid. τ_{PIV} is the finite time separation between two observations (separation time between image snapshots)

$Re = 520$, respectively, to obtain suitable particle displacement. Similarly, upon blockage insertion one hundred time-averaged single frame images were acquired at FR of 2,000 and FR 3,600 Hz at $Re = 320$ and $Re = 520$, respectively (Fig. 3b). Comparable FR to Echo PIV could not be applied as acquisition with the Photron SA-4 requires the use of pre-programmed FR at select intervals. Sufficient velocity convergence was achieved with 100 images both prior to and subsequent to blockage introduction of the downstream flow field. Resulting downstream FOV extent was $x/R = 3.4$ at both interrogating FR (Fig. 1b).

The dynamic velocity range (DVR) is defined as the ratio of the maximum velocity and the residual noise level of the correlation result (Eq. 3) (Son et al. 2002):

$$DVR = k_g \frac{U_{max}}{\sigma_{\Delta x} M_o \Delta t} \tag{3}$$

where k_g is the grid refinement ratio, U_{max} is the maximum velocity, M_o is the image magnification equal to 0.645 and Δt is FR^{-1}. Poelma et al. (2012) state an estimate of 0.1–0.2 pixels associated with the displacement uncertainty of the correlation result. The uncertainty in pixel displacement was thus set to 0.1 pixels where (Eq. 4):

$$\sigma_{\Delta x} = 0.1(d_e^2 + d_r^2)^{\frac{1}{2}} \tag{4}$$

where d_e is the diffraction limited diameter and d_r is the resolution of the camera (Table 2). Using 69.0 and 20 µm as the effective particle image diameter and resolution of the camera, respectively, $\sigma_{\Delta x} = 2.37$ µm and the recorded image diameter d_r was 71.9 µm or ~ 3.6 pixels. Resulting DVR using a grid refinement ratio of 3 ranged from 36 at 1,500 Hz to 45 at 3,600 Hz.

Dynamic spatial range (DSR) represents the ratio of the maximum to minimum resolvable scale (Eq. 5) (Son et al. 2002):

$$DSR = \frac{L_x/M_o}{U_{max} * \Delta t} \tag{5}$$

where L_x is the SA-4 CMOS pixel array dimension of 20.48 mm. Calculated DSR ranged from 192 at 3,600 Hz to 240 at 1,500 Hz.

Fastcam acquired images were imported into DaVis 8.1.3 and subjected to an equivalent cross-correlation procedure to that described above for Echo PIV. Images were masked to enable vector quantification from the centerline to the far wall to match Echo PIV analysis resulting in a final vector field of 31 radially spaced vectors and a final DPIV spatial vector grid of $\sim 0.21 \times 0.21$ mm^2. Smoothing was not applied to the final DPIV vector fields. Furthermore, DPIV measurements from the blockage outlet to $x/R = 0.15$ were omitted due to air bubble deposition immediately downstream of the blockage that led to cross-correlation degradation. Both DPIV individual vector fields and the final time-averaged vector fields were exported to MATLAB R2011a for post-processing.

2.4 Data analysis

Measurements acquired prior to blockage insertion were compared to known steady flow analytical theory using a single vector row instead of averaging all vector rows within our FOV. Specifically, centerline velocities and WSS quantified using the quadratic method (Eq. 6, Lou et al. 1993) were compared to Poiseuille:

$$\text{WSS} = \mu * \left(\frac{U_{x3}\text{dr}_2^2 - U_{x2}\text{dr}_3^2}{\text{dr}_3\text{dr}_2^2 - \text{dr}_2\text{dr}_3^2} \right) \quad (6)$$

where U_{x2} and U_{x3} are the second and third axial velocity measurement radially from the wall, dr_2 and dr_3 are their corresponding distances from the wall and μ is the dynamic viscosity. Flow downstream of the blockage was quantified through axial, negative axial, centerline and radial velocity profile comparisons that are critical predictors of resulting WSS patterns and in vivo stenosis severity. Velocities (u) and standard deviations (SD) were normalized to the peak inlet pre-blockage centerline velocity (U) corresponding to each Re.

3 Results

Echo PIV results are presented as a comparison to DPIV measurements at each Re. Comparison of Echo PIV and DPIV measurements to known steady flow analytical theory prior to blockage insertion is presented first followed by a comprehensive evaluation of downstream flow patterns. Measured post-blockage axial velocities, extent of negative axial velocities, centerline velocities and radial velocity profiles are compared and presented.

3.1 Pre-blockage measurement

Prior to blockage insertion, Poiseuille predicted radial velocity profiles were in close agreement with Echo PIV and DPIV measurements (Fig. 4a, b). Echo PIV measured centerline velocities at $Re = 320$ and $Re = 520$ were within 1 % of DPIV measured centerline velocities at both Re and displayed good agreement extending from the centerline to the wall (Fig. 4a, b). Time-averaged SD was elevated for all Echo PIV measurements with a near order of magnitude increase in close proximity to the wall. Both Echo PIV and DPIV measured WSS were within 5 % of Poiseuille at $Re = 320$ and $Re = 520$ (Fig. 4a, b). Integrated Echo flow rates were within 4 % of DPIV at both Re.

3.2 Post-blockage measurement

3.2.1 Axial velocities

Downstream axial velocity profiles are presented in Figs. 5 and 6 at $Re = 320$ and $Re = 520$, respectively. Presented values of axial extent represent the furthest downstream propagation of negative axial velocities despite discontinuities in recirculation zones. The extent of negative axial
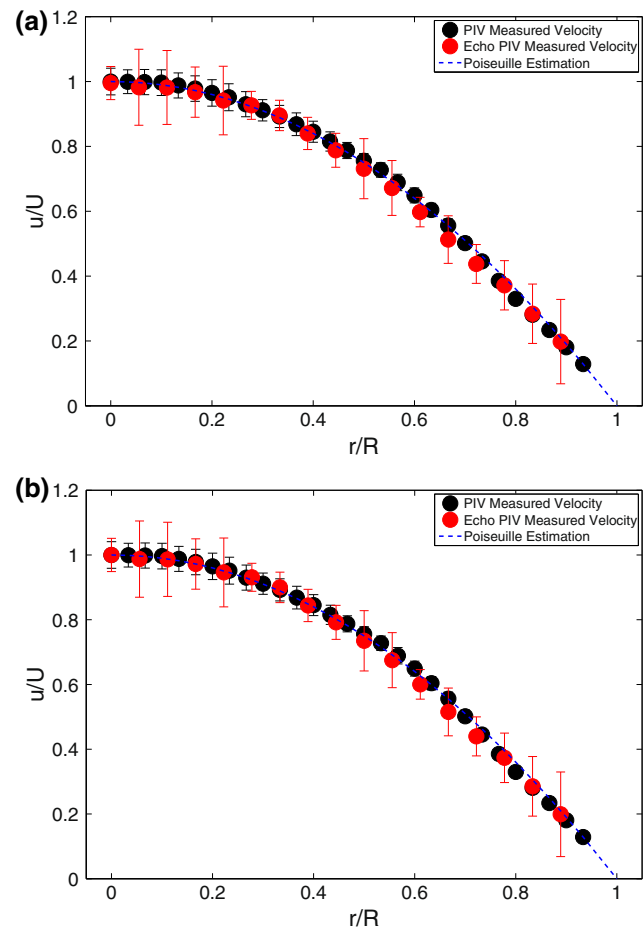
Fig. 4 Echo particle image velocimetry (Echo PIV) and digital particle image velocimetry (DPIV) measured radial velocity (±SD) profiles at Reynolds number (Re) = 320 (**a**) and Re = 520 (**b**) prior to the axisymmetric blockage insertion. Velocities were normalized to the peak centerline value at each Re

velocity propagation increased in relation to Re (Figs. 7, 8). Echo PIV measured negative axial velocities were found in discrete recirculation regions compared to DPIV (Figs. 7, 8). Echo PIV measured negative axial velocities at $Re = 320$ extended to $x/R = 2.35$ and $x/R = 1.43$ with maximum negative velocities of $u/U = -0.056$ and $u/U = -0.036$ at LD 64 and LD 128, respectively (Fig. 7a, b). Measured DPIV negative axial velocities propagated downstream to $x/R = 1.58$ with a maximum of $u/U = -0.082$ while expanding radially to $r/R = 0.833$ (Fig. 7c). Length of Echo PIV measured negative axial velocity propagation increased at $Re = 520$ to $x/R = 2.55$ and $x/R > 1.2$ (maximum extent of FOV) with maximum velocities of $u/U = -0.043$ and $u/U = -0.047$ at LD 64 and LD 128 (Fig. 8a, b). DPIV measured reattachment length was $x/R = 2.58$ at $Re = 520$ with maximum negative axial velocities and radial propagation of $u/U = -0.108$ and $r/R = 0.833$, respectively (Fig. 8c).
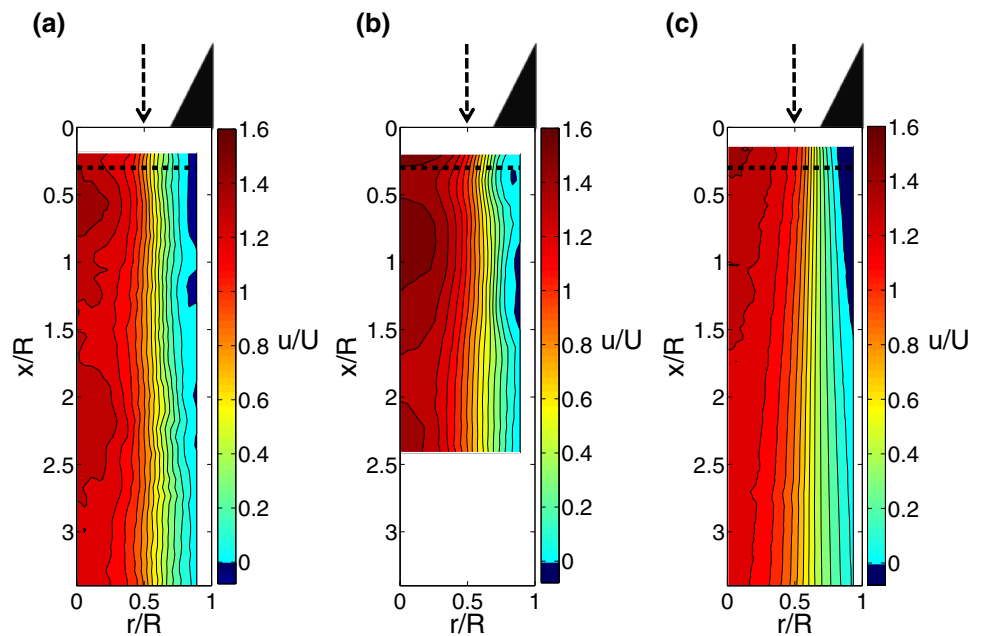
Fig. 5 Measured axial velocity profiles for echo particle image velocimetry (Echo PIV) line densities (LD) of 64 (**a**), 128 (**b**) and digital particle image velocimetry (DPIV) (**c**) extending downstream from a 50 % reduction by area axisymmetric blockage at Reynolds number (Re) = 320. Velocities were normalized to the peak inlet pre-blockage centerline value. The included *arrow and dashed black line* represent outlet flow direction from the stenosis and a distance of $x/R = 0.3$ from blockage outlet whereupon subsequent radial velocity profiles were compared, respectively (see Figs. 9, 10)

Fig. 6 Measured axial velocity profiles for echo particle image velocimetry (Echo PIV) line densities (LD) of 64 (**a**), 128 (**b**) and digital particle image velocimetry (DPIV) (**c**) extending downstream from a 50 % reduction by area axisymmetric blockage at Reynolds number (Re) = 520. Velocities were normalized to the peak inlet pre-blockage centerline value. The included *arrow and dashed black line* represent outlet flow direction from the stenosis and a distance of $x/R = 0.3$ from blockage outlet whereupon subsequent radial velocity profiles were compared, respectively (see Figs. 9, 10)
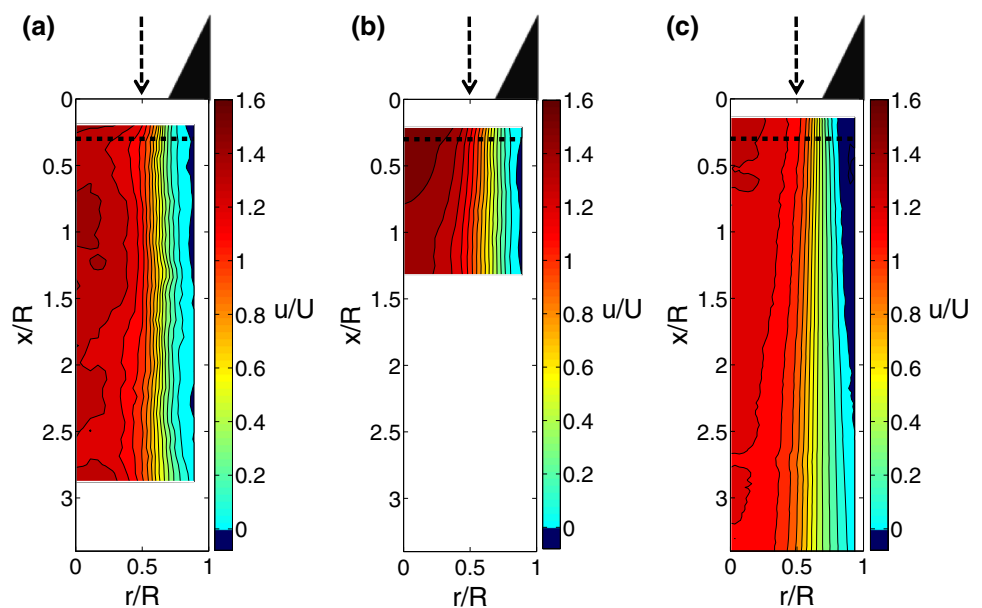
3.2.2 Centerline velocities

Maximum centerline velocities of $u/U = 1.44$ and $u/U = 1.51$ at LD 64 and LD 128, respectively, were measured by Echo PIV downstream of the blockage at $Re = 320$ (Fig. 9a). Corresponding maximum DPIV measured centerline velocity was $u/U = 1.42$ at $x/R = 0.19$ (Fig. 9a). Standard deviations were noticeably reduced at LD 128 (Fig. 9a). At $Re = 520$, maximum Echo PIV measured centerline velocities were $u/U = 1.4$ and $u/U = 1.51$ at $x/R = 0.19$ for LD 64 and LD 128,

respectively (Fig. 9b). DPIV measured maximum centerline velocity was $u/U = 1.35$ at $x/R = 0.19$ (Fig. 9b). Similar to $Re = 320$, LD 64 centerline velocity SD was elevated at all measurements downstream of the blockage (Fig. 9b).

3.2.3 Radial velocity profiles

Integrated post-blockage Echo PIV flow rates showed good agreement with both pre- and post-blockage DPIV values. Echo PIV measured radial velocity profiles at $Re = 320$
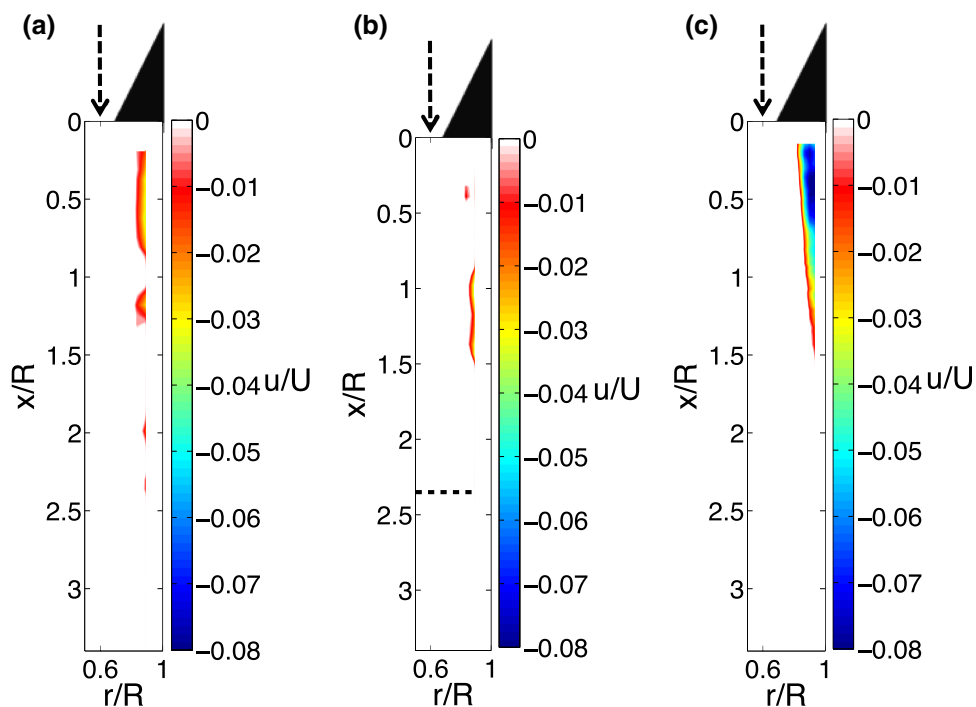
Fig. 7 Echo particle image velocimetry (Echo PIV) line densities (LD) of 64 (**a**), 128 (**b**) and digital particle image velocimetry (DPIV) (**c**) measured negative axial velocity propagation downstream of a 50 % reduction by area axisymmetric blockage at Reynolds number (*Re*) = 320. Velocities were normalized to the peak inlet pre-blockage centerline value. The included *arrow and dashed line* represent outlet flow direction from the stenosis and downstream extent of ultrasound field of view (FOV) at LD 128, respectively

Fig. 8 Echo particle image velocimetry (Echo PIV) line densities (LD) of 64 (**a**), 128 (**b**) and digital particle image velocimetry (DPIV) (**c**) measured negative axial velocity propagation downstream of a 50 % reduction by area axisymmetric blockage at Reynolds number (*Re*) = 520. Velocities were normalized to the peak inlet pre-blockage centerline value. The *included arrow and dashed line* represent outlet flow direction from the stenosis and downstream extent of ultrasound field of view (FOV) at LD 64 and 128
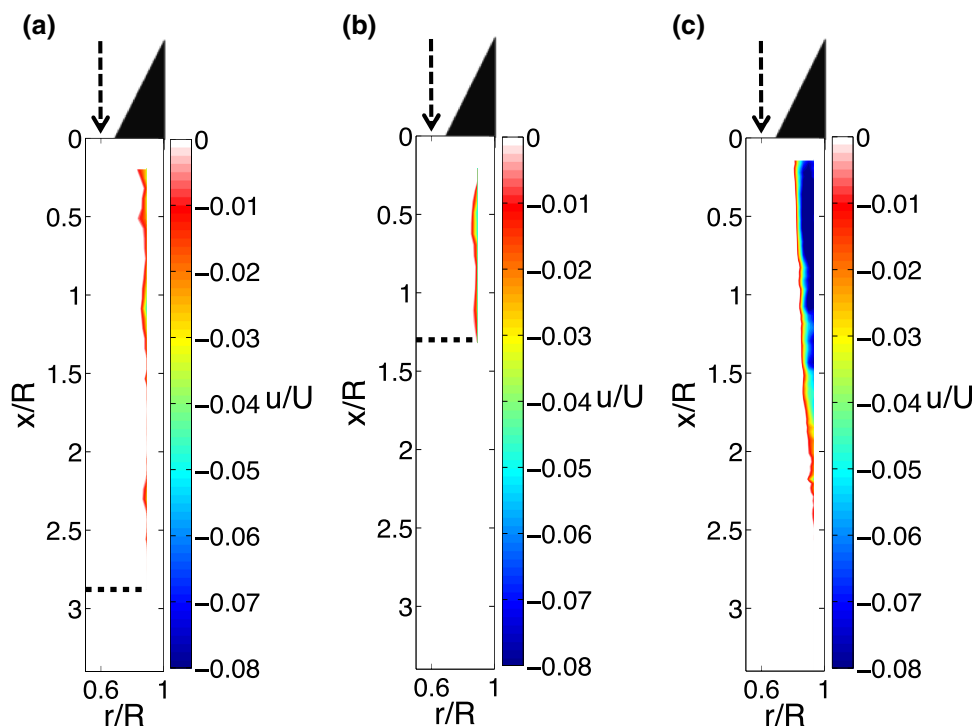
displayed good agreement with DPIV at $x/R = 0.3$ from the blockage outlet (Fig. 10a). Specifically, the Echo PIV measured centerline velocities located at $r/R = 0$ acquired at 64 LD and 128 LD were within 1 % of the corresponding DPIV measurement (Fig. 10a). Divergence from DPIV measurements were noted moving toward the shear layer where peak negative axial velocities at LD 64 and LD 128 were $u/U = -0.04$ and $u/U = -0.01$, that were $u/U = 0.03$ and $u/U = 0.06$ lower than measured by DPIV, respectively (Fig. 10a). Similar to centerline SD, SD was reduced at LD 128, specifically near the centerline and wall when normalized to local mean (Fig. 10b). At
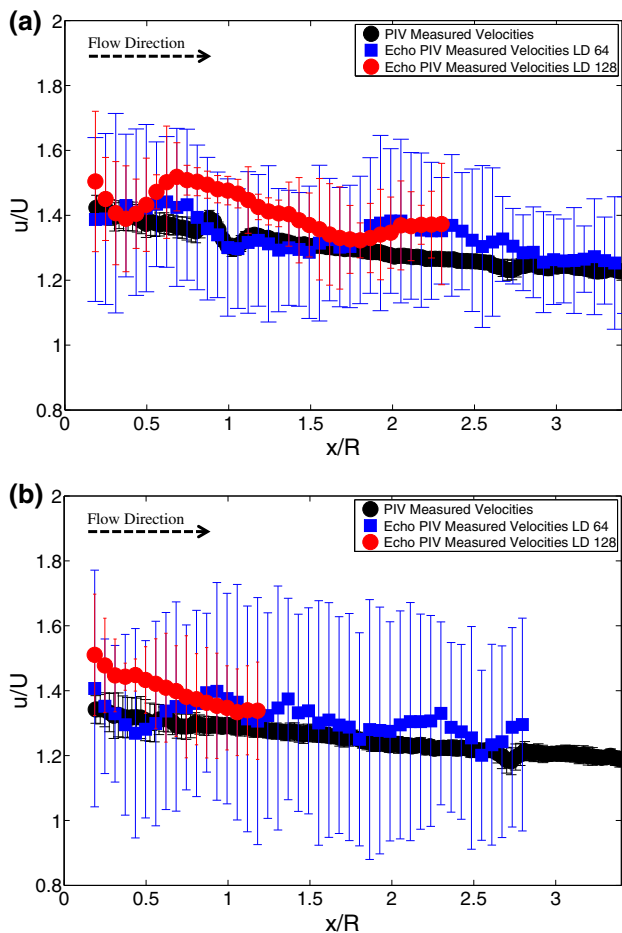
Fig. 9 Echo particle image velocimetry (Echo PIV) line densities (LD) of 64, 128 and digital particle image velocimetry (DPIV) measured centerline velocities (±SD) extending downstream from a 50 % axisymmetric blockage at Reynolds number (Re) = 320 (**a**) and Re = 520 (**b**). Velocities were normalized to the peak inlet pre-blockage centerline value for each Re

Fig. 10 Echo particle image velocimetry (Echo PIV) line densities (LD) of 64, 128 and digital particle image velocimetry (DPIV) measured radial velocity (±SD) profiles at a distance of x/R = 0.3 downstream of a 50 % reduction by area axisymmetric blockage at Reynolds number (Re) = 320 (**a**). Velocities were normalized to the peak inlet pre-blockage centerline value. Standard deviation of radial measurements were normalized as a function of local post-blockage mean velocity value (u) (**b**). Values with a ratio less than SD/u = 1.0 are displayed

Re = 520, centerline velocities were within 1 and 8 % of the DPIV measurement at LD 64 and LD 128, respectively (Fig. 11a). Maximum negative axial velocities of u/U = −0.01 and u/U = −0.02 were measured at LD 64 and LD 128 that were u/U = 0.07 and u/U = 0.06 lower than DPIV, respectively (Fig. 11a). Local SD was reduced using LD 128 with largest local SD for all measurements occurring in the shear layer and recirculation region (Fig. 11b).

4 Discussion

Although past work has quantified post-stenotic flow using Echo PIV, results were limited to centerline velocity and vector and contour map comparisons (Qian et al. 2011; Zhu
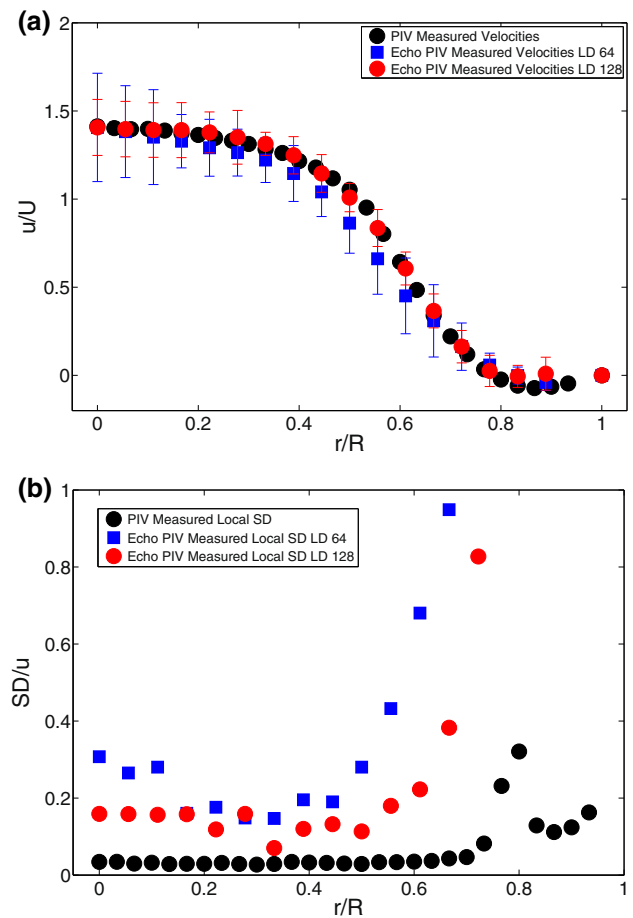
et al. 2011). Additionally, Echo PIV findings were compared to PWD and CFD that have important considerations when measuring complex flows, namely reliance on parabolic velocity profile extrapolation and accurate modeling of transitional/turbulent flows. The comprehensive evaluation of post-blockage induced flow has allowed us to demonstrate that Echo PIV does provide good quantitative centerline velocity agreement with DPIV, but that accurate characterization of recirculation zones is difficult due to reduced bubble penetration beyond the shear layer (see Fig. 12b). Caution must also be taken when using points near the wall for WSS quantification that show large SD in relation to their mean values. This can be remedied to an extent using ultrasound images with greater LD at a cost of reduced FOV.
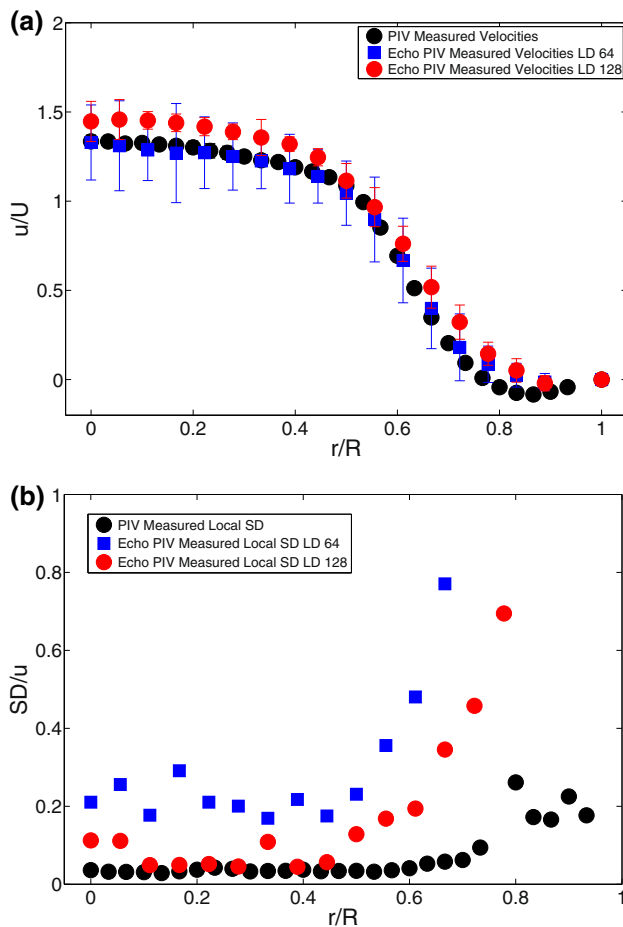
Fig. 11 Echo particle image velocimetry (Echo PIV) line densities (LD) of 64, 128 and digital particle image velocimetry (DPIV) measured radial velocity (±SD) profiles at a distance of $x/R = 0.3$ downstream of a 50 % reduction by area axisymmetric blockage at Reynolds number (Re) = 520 (**a**). Velocities were normalized to the peak inlet pre-blockage centerline value. Standard deviation of radial measurements were normalized as a function of local post-blockage mean velocity value (u) (**b**). Values with a ratio less than SD/u = 1.0 are displayed

4.1 Centerline velocity

Echo PIV presents itself as an attractive tool for in vivo flow measurement that uses readily available, affordable technology to characterize the flow under investigation. Centerline velocities measured prior to and after blockage insertion showed good agreement with DPIV at both Re and LD. However, noticeable reductions in SD at all measurement points at both Re were apparent using increased LD. Although decreased LD permits the use of high FR through an increase in sweep speed, lateral resolution is compromised degrading the presentation of ultrasound echoes. This was readily apparent through enhanced smearing and elongation of microbubbles that traversed the FOV at LD 64. Acquisition at low BLD (e.g., LD 64) increases the gap spacing between scan lines. To

generate a continuous ultrasound image, data must be interpolated between scan lines whereupon the degree of interpolation is a function of BLD. Furthermore, increased particle diameter is associated with a degradation of PIV measured displacement through a broadening of the cross-correlation peak (Kähler et al. 2005). Visual comparison of correlation peaks between LD 64 and LD 128 confirmed this with reduced correlation coefficients, broadening of the peak and enhanced secondary peaks at low LD. The reduced correlation quality through increased particle image diameter is likely responsible for the high SD of LD 64 measurements (Raffel et al. 2007). Line densities could be further increased than values here, but this does restrict the dynamic range of measurements through a reduction in FR. These findings do suggest, however, that Echo PIV flow quantification warrants the consideration of increased LD at a cost to FOV.

4.2 Near-wall flow patterns

Zhang et al. (2011) showed a good fit of in vitro wall shear rate measurements to DPIV at both near and far walls of a carotid artery model using a spatially averaged three-point polynomial fit. Large SD and overestimation compared to DPIV measurements were noted however, at the near-wall during diastolic deceleration (Zhang et al. 2011). Similarly, Poelma et al. (2012) found close agreement assuming Poiseuille flow and a parabolic fit, but cautioned against this approach in complex flows where reliable WSS measurement requires the use of points in close proximity to the wall. If using a three-point quadratic approach (Eq. 2), measurements between $r/R = 0.8$ and the wall would be used for WSS estimation (Figs. 10, 11). Although close agreement was found in non-blockage flow (Fig. 4), failure of Echo PIV to capture the full extent of negative axial velocity magnitude would underestimate negative WSS (Figs. 7, 8, 10, 11). Most concerning is the high SD as a function of local mean for measurements between $r/R = 0.6$ and the wall (Figs. 10b, 11b). This suggests that the use of instantaneous velocities for WSS estimation could greatly deviate from true values. The high near-wall SD does support the use of measurements toward the centerline (<0.6 r/R) for WSS estimation. However, in this scenario, near-wall values would contribute little to WSS resulting in an oversimplification of near-wall flow in complex environments. Given the results presented here, further refinement in near-wall measurement is required before proceeding to in vivo quantitative studies of WSS in complex flow environments. Of note, Poelma et al. (2012) concluded that a centroid-based displacement estimator reduces inherent bias associated with a Gaussian fit as used by DaVis 8.1.3. Reduction in the root-mean-square (RMS) of the residuals and improvement in the estimation of mean

velocity was noted for the centroid approach. Although Poelma et al. (2012) does provide initial insight, how the centroid method would perform in comparison to a Gaussian fit in complex flows is not immediately know, but does present itself as an attractive application in future Echo PIV studies when quantifying such environments.

Both Echo PIV and DPIV resolved post-blockage recirculation zones and strong shear layers that have been observed previously in vitro downstream of a 50 % by area stenotic constriction in steady flow (Ahmed and Giddens 1983). Flow patterns measured would be conducive to neointimal hyperplasia, possible thrombus formation and WSS patterns that would compromise local vessel homeostatic mechanisms (Malek et al. 1999; Berger and Jou 2000; Schirmer and Malek 2007). However, magnitude and extent of recirculation quantified by Echo PIV were reduced compared to DPIV that would marginalize near-wall flow patterns associated with potential atherosclerotic development. Similar underestimation of reversed flow was measured by Zhang et al. (2011) during flow deceleration in a model of the carotid bifurcation. This becomes particularly problematic as Re is increased and unsteady phenomena such as vortex shedding appear that alter local platelet kinetics and apply an additional force to the vessel wall that may contribute to plaque fatigue (Bluestein et al. 1999; Stroud et al. 2002; Varghese and Frankel 2003). Differences in effective window sizes (Echo PIV $\sim 0.33 \times 0.33$ mm^2, DPIV $\sim 0.21 \times 0.21$ mm^2) likely contributed to the disparities measured in the shear layer. The reduced spatial resolution of Echo PIV compared to DPIV necessitates the use of interrogation windows that envelop a larger lumen area that would preclude achieving the assumption of flow homogeneity. Although the effective window sizes could have been matched, velocity comparisons upon matching window overlap as presented here and not effective window size allows for the appreciation of the limitations of Echo PIV measurements in reference to an in vitro gold standard technique with superior spatial resolution capabilities.

Although resolution differences likely contributed to the recirculation discrepancies, it was visually observed that microbubble penetration beyond the shear layer to the recirculation zone was limited. To quantify this, Echo PIV and DPIV images were imported to NI LabView IMAQ 4.6.4. (National Instruments, Austin, TX), filtered and thresholded to generate well-contrasted images that were subsequently quantized into discrete bins centered at $x/R = 0.3$. The number of particles counted in each bin were summed for all image frames and averaged to produce an average particle count per bin that was normalized to the bin with the highest average count for each respective measurement approach. Prior to blockage insertion, a relatively uniform seeding concentration was noted from

the wall to $r/R = 0.2$ (Fig. 12a). Interestingly, low microbubble concentrations were found between $0 \leq r/R \leq 0.2$ that corresponded to Echo PIV measurements with high SD (Figs. 4, 12a). A precise reason as to the measured low concentrations is not immediately known. However, good agreement was found between Echo PIV and DPIV time-averaged velocity measurements where low shear strain rates would suggest particle displacement homogeneity within interrogation windows enveloping this spanwise range. Both tracer particles displayed similar behavior in the freestream velocity downstream of the blockage where low seeding numbers were found (Fig. 12b). Average tracer particle count increased radially moving toward the wall, peaking near the shear layer (Fig. 12b). Although average DPIV hollow glass sphere count decreased in the recirculation region, counts remained appreciably higher than freestream values. Alternatively, average Echo PIV contrast agent count decreased markedly in the
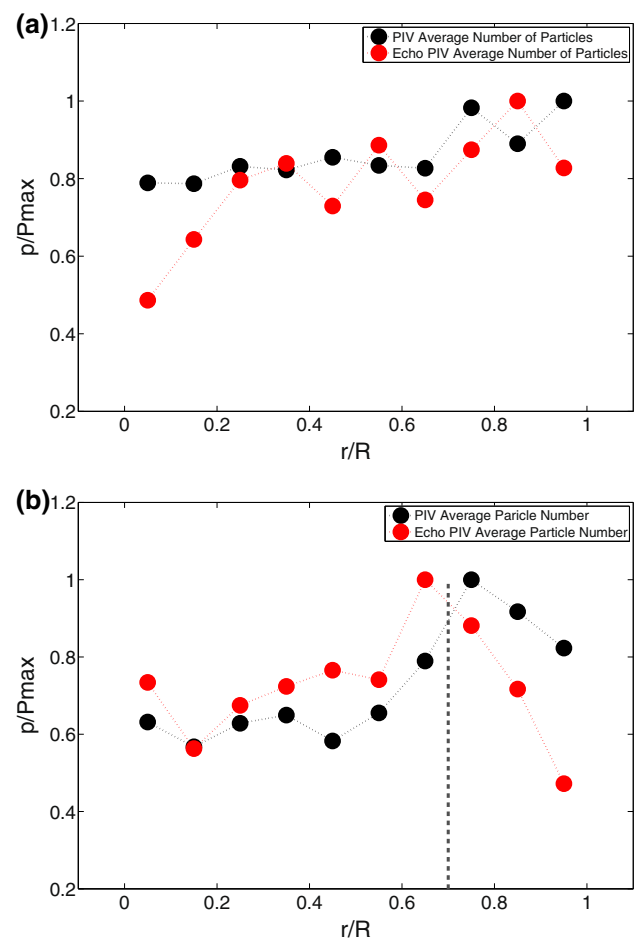

Fig. 12 Average number of particles (p) within respective radial bin locations pre (**a**) and post (**b**) blockage introduction centered at $x/R = 0.3$. Number of particles was normalized to the bin with the highest average number of particles ($P_{\max}$) for each respective measurement approach. Radial extent of blockage in tube lumen represented by *dashed line* at $r/R = 0.7$ (**b**)

recirculation region to counts lower than the freestream (Fig. 12b). The consequence of such a decrease in near-wall tracer particle counts would further limit the use of near-wall points to estimate WSS that would adversely affect such estimates using a quadratic or linear method. Similar to the high SD of near-wall downstream Echo PIV measurements, low particle count would necessitate the use of velocities at increased spanwise distance from the wall tending the resulting estimate to that of using Poiseuille based on the centerline velocity.

This behavioral response was surprising as it was expected that added microbubbles would faithfully follow the flow given the reduced diameter of Definity®. The Stokes numbers (St) for Definity® and the hollow glass spheres ranged between $\sim 6.5 \times 10^{-5}$–1.1×10^{-4} and 0.012–0.019 dependent on the finite time separation between images, respectively. It must be noted, however, that St calculation assumes particle rigidity. Values well below unity as calculated here for both tracer particles would suggest a dynamic equilibrium with the aqueous glycerol fluid. Indeed, Crowe et al. (1995) noted that in a vortex simulation of a plane mixing layer, particles with a $St = 0.1$ penetrated the vortical structures while particles of $St = 1$ accumulated along the edges of vortices. Similarly, in jet flow experiments using solid particles, those of $St = 1$–10 concentrated in high shear strain rate regions on the edge of the vortex while avoiding low shear strain rate regions of the vortex core (Crowe et al. 1995). It cannot be concluded for certain as to whether density differences between the tracer particles are responsible for the observed behaviors. Although a precise density for Definity® could not be sourced, Becher and Burns (2000) do note that the bubbles are neutrally buoyant suggesting that rise velocity is negligible. Comparable densities between Definity® and the surrounding fluid would suggest that added mass effects are not negligible. However, given that both tracer particles likely present with similar densities, added mass differences alone would fail to explain why Definity® poorly penetrates the shear layer.

The diameters of both particles would implicitly suggest rapid entrainment into large-scale flow structures, which in this instance is restricted to hollow glass spheres. It is speculated here given that St is much less than unity, the observed behavior results from body and dissimilar lift forces experienced brought upon by dissimilar outer shell construction. Definity® is composed of a flexible bilipid shell surrounding a perfluoropropane microbubble (Becher and Burns 2000). Strong lift forces resulting from the velocity gradient in the shear layer act upon the particles in the radial direction toward the freestream (Merzkirch 1987; Tropea et al. 2007). Deformable particles are subjected to an additional lift force due to their flexibility that may explain the decreased Definity® particle migration across

the shear layer in relation to the rigid spheres (Eckstein et al. 1977; Hur et al. 2011). Additionally, Hur et al. (2011) commented that lift forces increase in relation to deformability. Indeed, de Jong et al. (2002) presented appreciable differences in resonance frequency and hence enveloping shell stiffness across three ultrasound contrast agents. At a bubble diameter of 2 μm, Quantison™ with a spray-dried albumin shell and Sonovue™, encapsulated with a phospholipid shell presented with resonance frequencies of 45.1 MHz and 7.7 MHz, respectively (Becher and Burns 2000; de Jong et al. 2002). Although not presented, a similar resonance frequency for Definity® to that of Sonovue™ would be expected on account of comparable shell properties (Becher and Burns 2000). This presents an area for future work to measure if alternative ultrasound contrast agents (e.g., Quantison™, Sonovue™) that present with different outer shell properties respond with similar behavior. Swirling flows are also associated with a centrifugal force that radiates particles outward from the vortex core (Melling 1997). Lecuona et al. (2002) noted that inner zones of strong vortices showed reduced particle concentration that is subsequently heighted at radii outward from the vortex, limiting the integrity of measurements in these regions. It should be noted that seeding density of Echo PIV was reduced to that of DPIV, suggesting that increased seeding of Definity® may lead to enhanced penetration through the shear layer. Although a possibility, the goal of Echo PIV is to reduce seeding that is associated with conventional contrast imaging and speckle tracking techniques (Liu et al. 2008).

4.3 Study limitations

The use of steady flow conditions and a simplified axisymmetric stenotic geometry housed in a rigid tube neglected the inherent pulsatility and natural compliance associated with cardiovascular flows. Although these simplifications are not representative of in vivo conditions, we felt their inclusion did not diminish the consequence of our results to quantifying such flows. The failure of Echo PIV to accurately resolve steady flow recirculation has important consequences in the potential application of Echo PIV to in vivo separated flow measurement. Recirculation is certainly present downstream of in vivo stenotic vessels. Regardless then, of whether steady or pulsatile flow was used for this study, the finding of reduced microbubble penetration beyond the developed shear layer serves to highlight the caution one must take when using near-wall velocity measurements to infer critical hemodynamic metrics. Compliance does decrease with age while the use of rigid acrylic tubing ensured appropriate clarity and consistent dimensional tolerances (Peterson and Plesniak 2008; Walker et al. 2012). Measurement planes differed

between the two approaches with Echo PIV and DPIV data captured on sagittal and coronal planes, respectively. The deviation in measurement planes could be responsible for differences in the quantified flow fields. However, the use of an axisymmetric blockage was intended to remedy this issue while calculated Echo PIV and DPIV flow rates through velocity integration were in close agreement. Furthermore, the necessity of two measurements planes prevented simultaneous acquisition of Echo PIV and DPIV images. This should have had limited bearing on our final results as pump performance and temperature were consistent across all trials.

Blood was represented by a Newtonian analog. Although an appropriate assumption in the largest arteries of the vasculature where shear strain rates are high, the consideration of nonlinear viscous behavior is warranted in separated flows (Walker et al. 2012). Based on flow patterns measured here, we would expect a dampening of recirculation length and subsequent reductions in peak centerline velocities (see Walker et al. 2012). Whether Echo PIV would accurately resolve the reduced recirculation zones is the subject of future work, but based on findings presented here, accurate quantification may be difficult due to poor bubble penetration beyond the shear layer in close proximity to the blockage outlet.

Two-dimensional Echo PIV and DPIV image snapshots acquired in separated flow environments are subjected to enhanced signal degeneration from out of plane motion. Although not of major concern at Re measured here, use of two-dimensional Echo PIV and DPIV does become problematic as Re is increased and three-dimensional flow becomes more prevalent (Choi and Barakat 2005). This advocates for the use of three-dimensional Echo PIV; however, current three-dimensional ultrasound probes are cumbersome and associated with low FR. With that in mind, stereoscopic Echo PIV does present itself as an attractive direction for immediate development.

5 Conclusions

Results presented here represent a comprehensive evaluation of downstream blockage flow patterns quantified by Echo PIV and DPIV interrogation. Although a simplified model was used to represent arterial flow conditions, our findings of Echo PIVs inability to accurately resolve separated flows are nonetheless translatable to observed downstream stenotic flow patterns in vivo. Echo PIV measured centerline velocities were found to be in good agreement with DPIV although SD was elevated at all measurement points. Standard deviations decreased when using higher ultrasound LD that improves lateral resolution; however, maintenance of FR at high LD requires a

reduction in FOV. Similarly, radial velocity profiles showed close agreement to DPIV with the largest discrepancies confined to the shear layer and recirculation zone. Most concerning was the large SD as a function of local mean velocity at radial points near the wall. This suggests that instantaneous measurements of near-wall velocity used for WSS deviation may deviate largely from true values and supports the use of velocity measurements toward the freestream of the flow. However, WSS measurements reliant on velocities toward the freestream would oversimplify near-wall flow patterns in complex environments. The findings of this work suggest that further refinement in near-wall measurements is required before proceeding to in vivo quantification of complex flow. Previous work demonstrated that a centroid-based estimator reduced RMS and improved mean velocity estimation compared to a traditional Gaussian peak fit approach. However, whether this approach improves WSS estimates in complex flow remains unknown, but does suggest that its use is warranted in future Echo PIV studies quantifying such flow environments.

Echo PIV and DPIV quantified negative axial velocities, however, spatial extent and magnitude were reduced in Echo PIV measurements. Past Echo PIV work on distal blockage flow commented on the lack of resolved recirculation although no precise reason for this behavior was presented. Visual observations of our flow noted a lack of Definity® echo contrast penetration beyond the shear layer radially toward the wall that was confirmed through an average particle count. This was unexpected, as the small particle diameter and St much less than unity would suggest rapid particle entrainment into large-scale flow structures. It is suggested that lift and centrifugal forces associated with shear layer and recirculation, respectively, are likely partially responsible for this observed behavior with a heightened response in deformable particles. Lift force is related to deformability that suggests a detailed separated flow evaluation is warranted of multiple contrast agents that present with different magnitudes of shell flexibility.

References

Ahmed SA, Giddens DP (1983) Velocity measurements in steady flow through axisymmetric stenoses at moderate Reynolds numbers. J Biomech 16:505–516
Becher H, Burns PN (2000) Handbook of contrast echocardiography: left ventricular function and myocardial perfusion. Springer

Berger SA, Jou L-D (2000) Flows in stenotic vessels. Annu Rev Fluid Mech 32:347–382

Beulen B, Bijnens N, Rutten M, Brands P, van de Vosse F (2010a) Perpendicular ultrasound velocity measurements by 2D cross-correlation of RF data. Part A: validation in a straight tube. Exp Fluids 49:1177–1186

Beulen B, Bijnens N, Rutten M, Brands P, van de Vosse F (2010b) Perpendicular ultrasound velocity measurements by 2D cross-correlation of RF data. Part B: volume flow estimation in curved vessels. Exp Fluids 49:1219–1229

Bluestein D, Gutierrez C, Londono M, Schoephoerster RT (1999) Vortex shedding in steady flow through a model of an arterial stenosis and its relevance to mural platelet deposition. Ann Biomed Eng 27:763–773

Bohs LN, Frimel BH, Trahey GE (1995) Experimental velocity profiles and volumetric flow via two-dimensional speckle tracking. Ultrasound Med Biol 21:885–898

Bohs LN, Geiman BJ, Anderson ME, Gebbart SC, Trahey GE (2000) Speckle tracking for multi-dimensional flow estimation. Ultrasonics 38:369–375

Choi HW, Barakat AI (2005) Numerical study of the impact of non-Newtonian blood behavior on flow over a two-dimensional backward facing step. Biorheology 42:493–509

Crowe CT, Troutt TR, Chung JN (1995) Particle interactions with vortices. In: Green SI (ed) Fluid vortices. Kluwer Academic Publishers, Dordrecht, pp 829–861

Curry TS, Dowdey JE, Murry RC Jr (1990) Christensen's physics of diagnostic radiology. Lippincott Williams and Wilkins, Philadelphia

de Jong N, Bouakaz A, Ten Cate FJ (2002) Contrast harmonic imaging. Ultrasonics 40:567–573

Dobson G, Maher N, Petrasek P, Johnston C (2007) Diastolic rotational flow in the aortic arch. Can J Anesth 54:1017–1018

Dobson G, Johnston CR, Walker A (2009) Strut-induced flow separation in an endostent. Can J Anesth 56:257–258

Durst F, Ray S, Ünsal B, Bayoumi A (2005) The development lengths of laminar pipe and channel flow. J Fluids Eng 127:1154–1160

Eckstein EC, Bailey DG, Shapiro AH (1977) Self-diffusion of particles in shear flow of a suspension. J Fluid Mech 79:191–208

Hochareon P, Manning KB, Fontaine AA, Tarbell JM, Deutsch S (2004) Wall shear-rate estimation within the 50 cc Penn State artificial heart using particle image velocimetry. J Biomech Eng 126:431–437

Hong G-R, Pedrizzetti G, Tonti G, Li P, Wei Z, Kim JK, Baweja A, Liu S, Chung N, Houle H, Narula J, Vannan MA (2008) Characterization and quantification of vortex flow in the human left ventricle by contrast echocardiography using vector particle image velocimetry. JACC Cardiovasc Imaging 1:705–717

Hur SC, Henderson-MacLennan NK, McCabe ERB, Di Carol D (2011) Deformability-based cell classification and enrichment using inertial microfluidics. Lab Chip 11:912–920

Kähler CJ, McKenna R, Scholz U (2005) Wall-shear-stress measurements at moderated Re-numbers with single pixel resolution using long distance μ-PIV: an accuracy assessment. Pasadena CA, USA: 6th International Symposium on Particle Image Velocimetry. pp 1–12

Kähler CJ, Scholz U, Ortmanns J (2006) Wall-shear-stress and near-wall turbulence measurements up to single pixel resolution by means of long-distance micro-PIV. Exp Fluids 41:327–341

Kheradvar A, Houle H, Pedrizzetti G, Tonti G, Belcik T, Ashraf M, Lindner JR, Gharib M, Sahn D (2010) Echocardiographic particle image velocimetry: a novel technique for quantification of left ventricular blood vorticity pattern. J Am Soc Echocardiogr 23:86–94

Kim HB, Hertzberg J, Lanning C, Shandas R (2004a) Noninvasive measurements of steady and pulsating velocity profiles and shear rates in arteries using echo PIV: In vitro validation studies. Ann Biomed Eng 32:1067–1076

Kim HB, Hertzberg JR, Shandas R (2004b) Development and validation of echo PIV. Exp Fluids 36:455–462

Ku D (1997) Blood flow in arteries. Annu Rev Fluid Mech 29:399–434

Lecuona A, Ruiz-Rivas U, Nogueira J (2002) Simulation of particle trajectories in a vortex-induced flow: application to seed-dependent flow measurement. Meas Sci Technol 13:1020–1028

Liu L, Zheng H, Williams L, Zhang F, Wang R, Hertzberg J, Shandas R (2008) Development of a custom-designed echo particle image velocimetry system for multi-component hemodynamic measurements: system characterization and initial experimental results. Phys Med Biol 53:1397–1412

Lou Z, Wang W-J, Stein PD (1993) Errors in the estimation of arterial wall shear rates that result from curve fitting of velocity profiles. J Biomech 26:383–390

Malek AM, Alper SL, Izumo S (1999) Hemodynamic shear stress and its role in atherosclerosis. JAMA 282:2035–2042

Melling A (1997) Tracer particles and seeding for particle image velocimetry. Meas Sci Technol 8:1406–1416

Merzkirch W (1987) Flow visualization. Academic Press Inc., London

Meunier P, Leweke T (2003) Analysis and treatment of errors due to high velocity gradients in particle image velocimetry. Exp Fluids 35:408–421

Moore JE Jr, Ku DN, Zarins CK, Glagov S (1992) Pulsatile flow visualization in the abdominal aorta under differing physiological conditions: implications for increased susceptibility to atherosclerosis. J Biomech Eng 114:391–397

Niu L, Qian M, Wan K, Yu W, Jin Q, Ling T, Gao S, Zheng H (2010) Ultrasonic particle image velocimetry for improved flow gradient imaging: algorithms, methodology and validation. Phys Med Biol 55:2103–2120

Niu L, Qian M, Yan L, Yu W, Jiang B, Jin Q, Wang Y, Shandas R, Liu X, Zheng H (2011) Real-time texture analysis for identifying optimum microbubble concentration in 2-D ultrasonic particle image velocimetry. Ultrasound Med and Biol 37:1280–1291

Peterson SD, Plesniak MW (2008) The influence of inlet velocity profile and secondary flow on pulsatile flow in a model artery with stenosis. J Fluid Mech 616:263–301

Poelma C, Mari JM, Foin N, Tang M-X, Krams R, Caro CG, Weinberg PD, Westerweel J (2011) 3D flow reconstruction using ultrasound PIV. Exp Fluids 50:777–785

Poelma C, van der Mijle RME, Mari JM, Tang M-X, Weinberg PD, Westerweel J (2012) Ultrasound imaging velocimetry: toward reliable wall shear stress measurements. Eur J Mech B/Fluids 35:70–75

Qian M, Niu L, Wang Y, Jiang B, Jin Q, Jiang C, Zheng H (2010) Measurement of flow velocity fields in small vessel-mimic phantoms and vessels of small animals using micro ultrasonic particle image velocimetry. Phys Med Biol 55:6069–6088

Qian M, Song R, Niu L, Chen L, Zheng H (2011) Two-dimensional flow study in a stenotic artery phantom using ultrasonic particle image velocimetry. Boston, MA, USA: 33rd Annual International Conference of the IEEE EMBS, pp 563–566

Raffel M, Willert C, Wereley S, Kompenhans J (2007) Particle image velocimetry: a practical guide. Springer, Berlin

Schirmer CM, Malek AM (2007) Wall shear stress gradient analysis within an idealized stenosis using non-Newtonian flow. Neurosurgery 61:855–864

Sengupta PP, Khandheria BK, Korinek J, Jahangir A, Yoshifuku S, Milosevic I, Belohlavek M (2007) Left ventricular isovolumic flow sequence during sinus and paced rhythms: new insights from use of high-resolution Doppler and ultrasonic digital particle image velocimetry. J Am Coll Cardiol 49:899–908

Son SY, Kihm KD, Han J-C (2002) PIV flow measurements for heat transfer characterization in two-pass square channels with smooth and 90° ribbed walls. Int J Heat Mass Transfer 45:4809–4822

Stroud JS, Berger SA, Saloner D (2002) Numerical analysis of flow through a severely stenotic carotid artery bifurcation. J Biomech Eng 124:9–20

Theunissen R, Scarano F, Riethmuller ML (2007) An adaptive sampling and windowing interrogation method in PIV. Meas Sci Technol 18:275–287

Tropea C, Yarin AL, Foss JF (2007) Springer handbook of experimental fluids mechanics. Springer, Berlin

Udesen J, Gran F, Hansen KL, Jensen JA, Thomsen C, Nielsen MB (2008) High frame-rate blood vector velocity imaging using plane waves: simulations and preliminary experiments. IEEE Trans Ultrason Ferroelectr Freq Control 55:1729–1743

Varghese SS, Frankel SH (2003) Numerical modeling of pulsatile turbulent flow in stenotic vessels. J Biomech Eng 125:445–460

Walburn FJ, Sabbah HN, Stein PD (1981) Flow visualization in a mold of an atherosclerotic human abdominal aorta. J Biomech Eng 103:168–170

Walker AM, Johnston CR, Rival DE (2012) The quantification of hemodynamic parameters downstream of a Gianturco zenith stent wire using Newtonian and non-Newtonian analog fluids in a pulsatile flow environment. J Biomech Eng 134:111001

Wootton DM, Ku DN (1999) Fluid mechanics of vascular systems, diseases, and thrombosis. Annu Rev Biomed Eng 1:299–329

Xiong FL, Chong CK (2007) PIV-validated numerical modeling of pulsatile flows in distal coronary end-to-side anastomoses. J Biomech 40:2872–2881

Young DF, Munson BR, Okiishi TH, Huebsch WW (2007) A very brief introduction to fluid mechanics, 4th edn. Wiley, Hoboken

Zhang F, Lanning C, Mazzaro L, Rech B, Chen J, Chen SJ, Shandas R (2008) Systematic validation of echo particle image velocimetry technique using a patient-specific carotid bifurcation model. Beijing, China: 2008 IEEE International Ultrasonics Symposium, pp 9–12

Zhang F, Lanning C, Mazzaro L, Barker AJ, Gates PE, Strain WD, Fulford J, Gosling OE, Shore AC, Bellenger NG, Rech B, Chen J, Chen J, Shandas R (2011) In vitro and preliminary in vivo validation of echo particle image velocimetry in carotid vascular imaging. Ultrasound Med Biol 37:450–464

Zheng H, Liu L, Williams L, Hertzberg JR, Lanning C, Shandas R (2006) Real time multicomponent echo particle image velocimetry technique for opaque flow imaging. Appl Phys Lett 88:261915

Zhu H, Qian M, Zou Y, Song R, Niu L, Jiang B, Guang Q, Zheng H (2011) The validation of Echo-PIV technique used in a stenosis model. Wuhan, China: the 5th International Conference on Bioinformatics and Biomedical Engineering (ICBBE 2011), pp 1–4